

**Mapping variations in bedrock weathering with slope aspect under a sedimentary ridge-valley system using near-surface geophysics and drilling**

Berit M. Hudson Rasmussen<sup>1</sup>, Mong-Han Huang<sup>1</sup>, W. Jesse Hahm<sup>2</sup>, Daniella M. Rempe<sup>3</sup>, David Dralle<sup>4</sup>, and Mariel D. Nelson<sup>3</sup>

<sup>1</sup>Department of Geology, University of Maryland, College Park, MD, USA,

<sup>2</sup>Department of Geography, Simon Fraser University, Burnaby, BC, Canada,

<sup>3</sup>Department of Geosciences, Jackson School of Geosciences, The University of Texas at Austin, Austin, TX, USA,

<sup>4</sup>Pacific Southwest Research Station, United States Forest Service, Albany, CA, US

**Contents of this file**

Figures S1 to S13

Tables S1 to S2

**Introduction**

Text S1 describes seismic velocity results not shown in the main text.

Figure S1 shows seismic line 2 results parallel to the bedding.

Figure S2 shows seismic line 3 results perpendicular to the bedding.

Figure S3 compares velocity profile with seismic velocity surveyed parallel or perpendicular to the bedding.

Figure S4 shows seismic lines 4 and 5 result along two maximum hillslope descend profiles.

Figure S5 shows seismic line 9 results perpendicular the bedding and across the main ridge.

Figure S6 shows seismic lines 10 and 11 results along the MH2 channel.

Figure S7 compares the critical zone structure for north- and south-facing hillslopes for lines 4 and 5, respectively.

Figure S8 compares weathering thickness on north- and south-facing hillslopes for line 6.

Figure S9 compares weathering thickness between north- and south-facing hillslopes of MH2, MH3, MH7, and MH8 based on interface 3 property.

Figure S10 shows a 1D porosity model for MH3R (Line 7).

Figure S11 shows a 1D porosity model for MH2R (Line 7).

Figure S12 compares 1D velocity profiles between mean west- and east-facing hillslopes of lines 8 and 9.

Figure S13 shows an average porosity with depth for the MH7R ridgetop.

Figure S14 shows the topography of interface 3 along north or south facing hills.

Table S1 lists the model parameters used for the seismic inversion.

Table S2 lists the elastic moduli for minerals used in the rock physics model.

## **Supplementary Text S1 – Summary of seismic velocity models (lines 3, 4, 5, 9)**

### **S1.1 MH7R Bedding-Perpendicular (Line 3)**

The low-velocity material of the bedding-perpendicular profile (Line 3; **Figure S2**) is generally faster than material in the same depth range of the bedding-parallel profile (**Figures 4, S1**). CoV is  $< 20\%$  almost everywhere above the deepest raypath, indicating consistency of velocity distribution between model ensembles (**Figure S2b**). The mean vertical gradient is lower than that of the bedding-parallel survey line, indicating a more gradual increase in velocity with depth (**Figure S2c**). The highest gradients ( $> 500$  m/s/m) are located below the channel. 1D velocity at the intersection point with bedding-parallel Line 1 indicates an overall similar profile, however Line 3 is slightly faster above a 6m depth (**Figure S3**). Similar to Lines 1 and 2, we do not reach high-velocity material below the MH7R ridgetop in this survey line.

### **S1.2 MH8 North-Facing Slope (Line 4) and MH7 South-Facing Slope (Line 5)**

Lines 4 (north-facing) and 5 (south-facing) are traced roughly perpendicular to the topographic contour lines to capture the steepest descent of the hillslope. Both survey lines show upslope-thickening weathering with a 30 m-thick weathered zone at the ridgetop (**Figure S4a,c**). The two slopes appear to have a similar thickness of low-velocity material, although the south-facing slope has considerably thinner mid-velocity (1000-3000 m/s) material. Velocity appears to increase more gradually below the north-facing slope and increases more rapidly on the south-facing slope. There is  $V_p > 4000$  m/s visible more than halfway up the south-facing slope, faster than is resolved in Line 1. Line 5 also resolves deeper ( $\sim 35$  m) below the MH7R ridge than Line 1 (only  $\sim 15$  m), possibly due to a longer maximum source-receiver distance for Lines 4 and 5.

### **S1.3 MH2R Perpendicular (Line 9)**

Three boreholes at MH2R are within 10 m of Line 9: MH3-W5, MH3-W7, and MH3-W8. CoV is high ( $> 50\%$ ) below the ridgetop, but along the slopes, we can resolve up to 30-40 m depth. Velocity gradient is once again highest at the channels and is generally  $< 200$  m/s/m elsewhere (**Figure S5a**). Similar to Line 8, velocity appears mostly sub-parallel to the topography (**Figure 7**). The low-velocity layer is uniformly 6-8 m thick along the east-facing slope of the MH2R perpendicular profile, with the exception of the eastern channel where it is  $< 3$  m thick. The middle-velocity layer is more variable, increasing to  $> 10$  m thick where the slope angle is most gradual, and thinning where the hillslope is steepest. The mid-velocity layer is nearly absent at the eastern channel, but it is still several meters thick at the western channel.

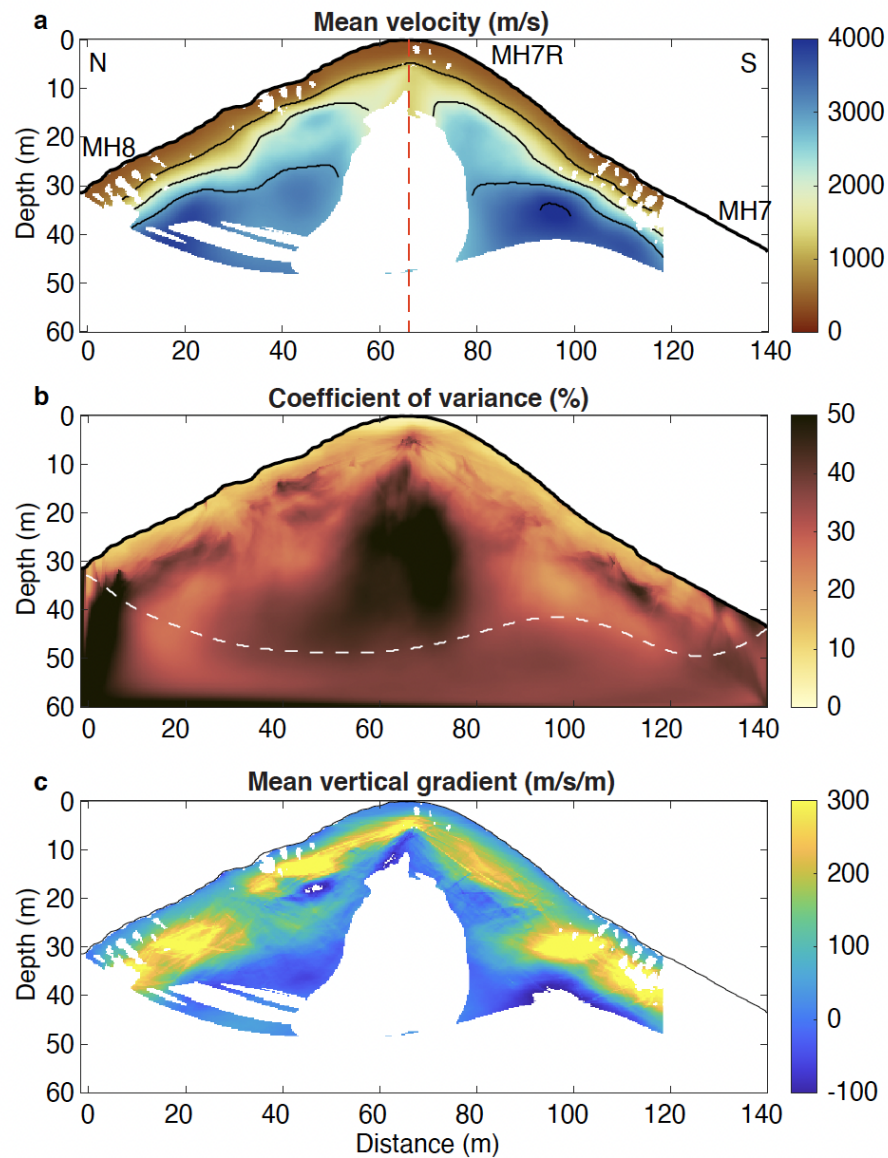


**Figure S1.** Results of Line 2 (a-c) inversion using THB rj-MCMC (Huang et al., 2021). (a) Mean velocity model with contour lines at 1000, 2000, 3000, and 4000 m/s. The model is masked out where no geophones are present (edges of survey), below the deepest raypath, and where coefficient of variation (CoV; standard deviation/mean velocity  $\times 100$ )  $> 30\%$ . The vertical dashed line highlights the locations of borehole MH7-W1. The same line also indicates the intersection point of Line 2 with Line 1 (see Figure 1b). (b) Percent CoV with the deepest raypath as the white dashed line. (c) Mean vertical velocity gradient (m/s/m).

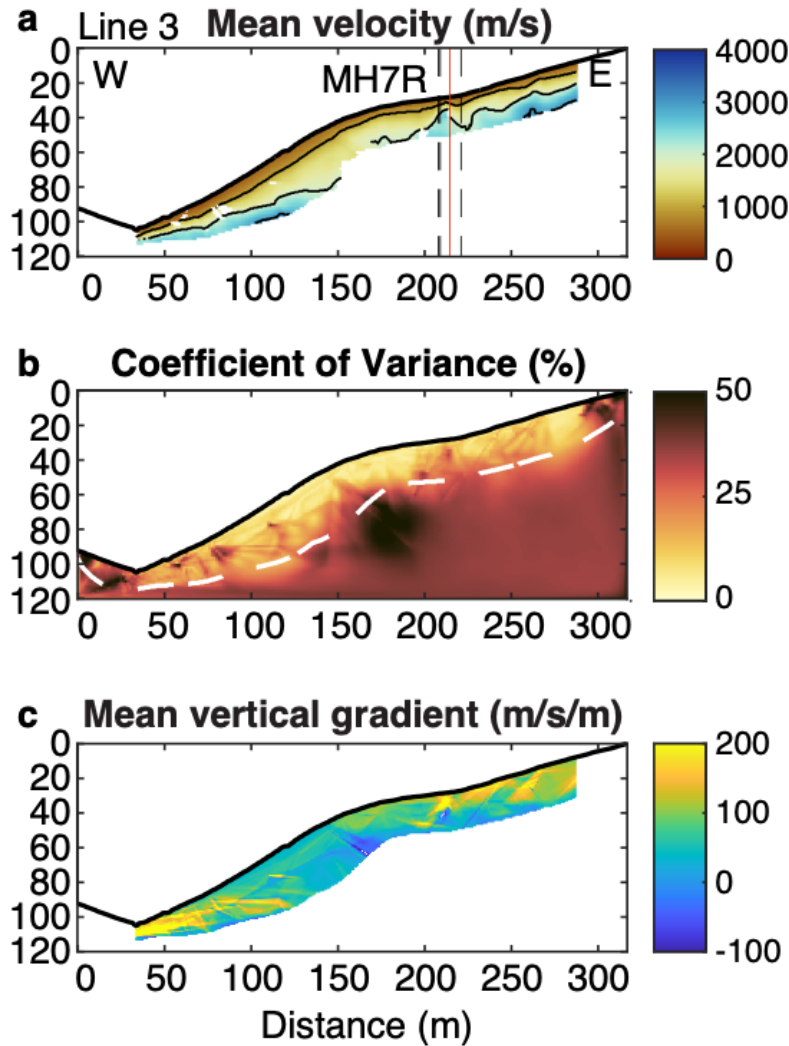


**Figure S2.** Results of Line 3 (a-c) inversion using THB rj-MCMC (Huang et al., 2021). (a) Mean velocity model with contour lines at 1000, 2000, 3000, and 4000 m/s. The model is masked out where no geophones are present (edges of survey), below the deepest raypath, and where coefficient of variation  $CoV > 30\%$ . Vertical dashed lines highlight the locations of boreholes within 10 m of the survey line. From west to east, these include boreholes MH7-W2, MH7-W3, and MH7-W1. The orange vertical line indicates the intersection point of Lines 1 and 3. (b) Percent  $CoV$  with the deepest raypath as the white dashed line. (c) Mean vertical velocity gradient (m/s/m).

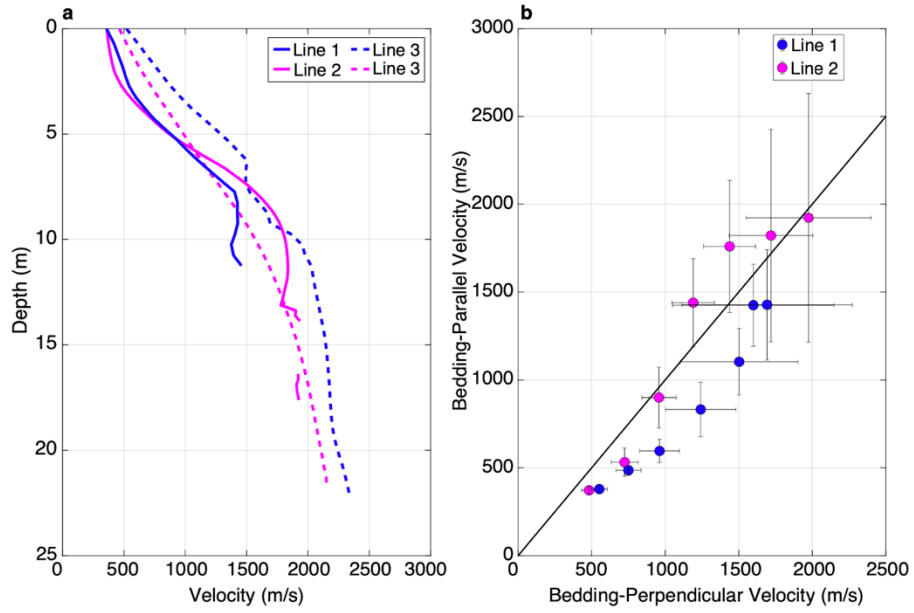


**Figure S3.** Velocity with depth at the intersection points of bedding-parallel and bedding-perpendicular survey lines for MH7R. **(a)** Solid and dashed lines show the velocity for bedding-parallel and bedding-perpendicular lines, respectively. **(b)** Bedding-perpendicular velocity vs bedding-parallel velocity. Blue circles represent the velocities at the intersection of Lines 1 and 3, and pink circles represent the velocities at the intersection of Lines 2 and 3.

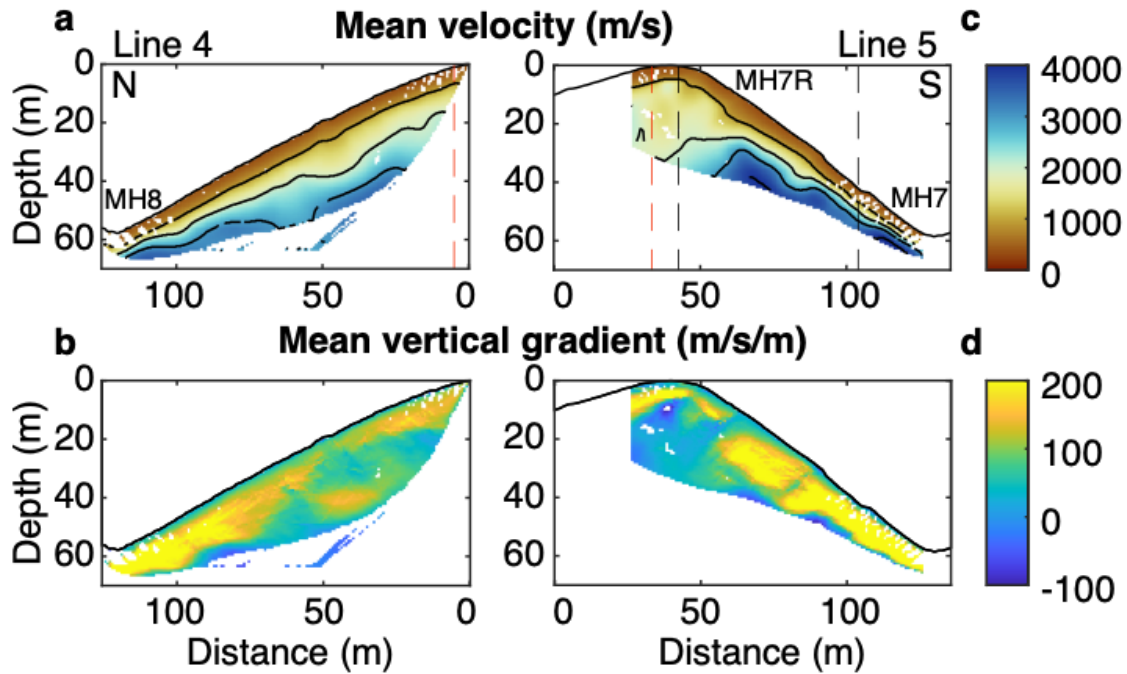


**Figure S4.** Results of Line 4 (a-b) and Line 5 (c-d) inversions. (a,c) Mean velocity model with contour lines at 1000, 2000, 3000, and 4000 m/s. The model is masked out below the deepest raypath and where CoV > 30%. Black dashed lines highlight the locations of boreholes within 10 m of the survey line (borehole MH7-W2 for Line 4; boreholes MH7-W2, MH7-W3, and MH7-W4 for Line 5). Lines 4 and 5 intersect at the MH7-W2 borehole (red dashed line). (b,d) Mean vertical velocity gradient (m/s/m).

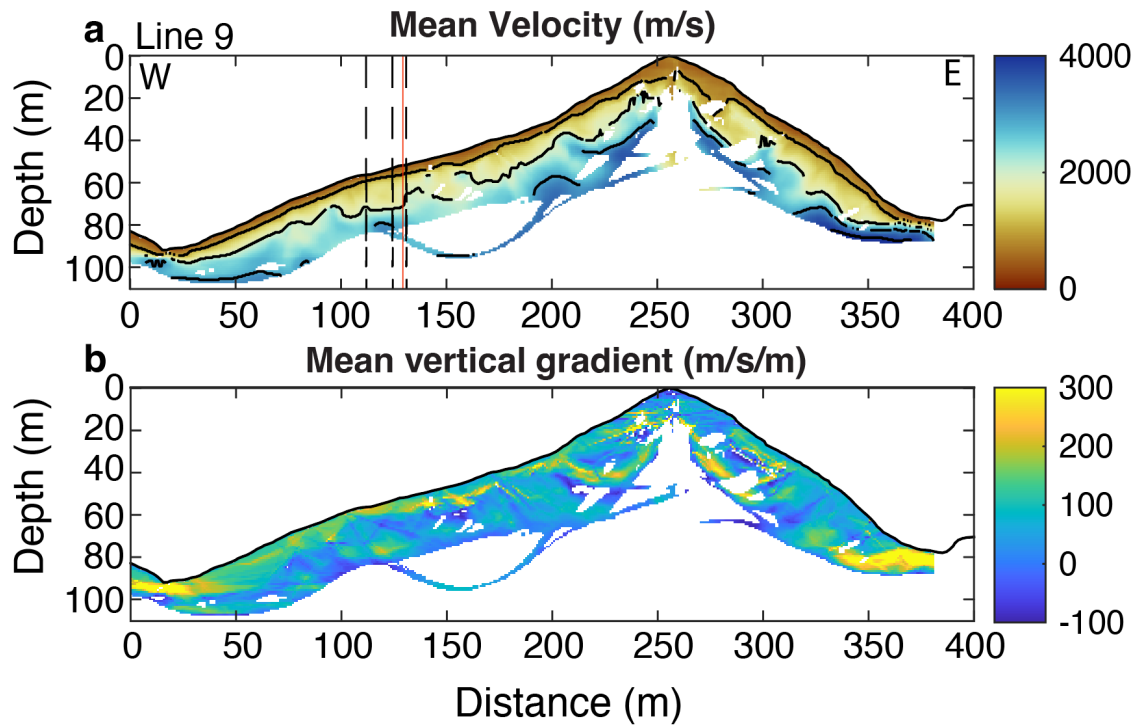


**Figure S5.** Results of Line 9 inversion. **(a)** Mean velocity model with contour lines at 1000, 2000, 3000, and 4000 m/s. The model is masked out below the deepest raypath and where CoV > 40%. Black dashed lines highlight the locations of boreholes within 10 m of the survey line. From west to east, these include boreholes MH3-W8, MH3-W7, and MH3-W5. The orange vertical line indicates the intersection point with Line 7. **(b)** Mean vertical gradient (m/s/m). Note the gradient color scale ranges from -100 to 300 m/s/m.

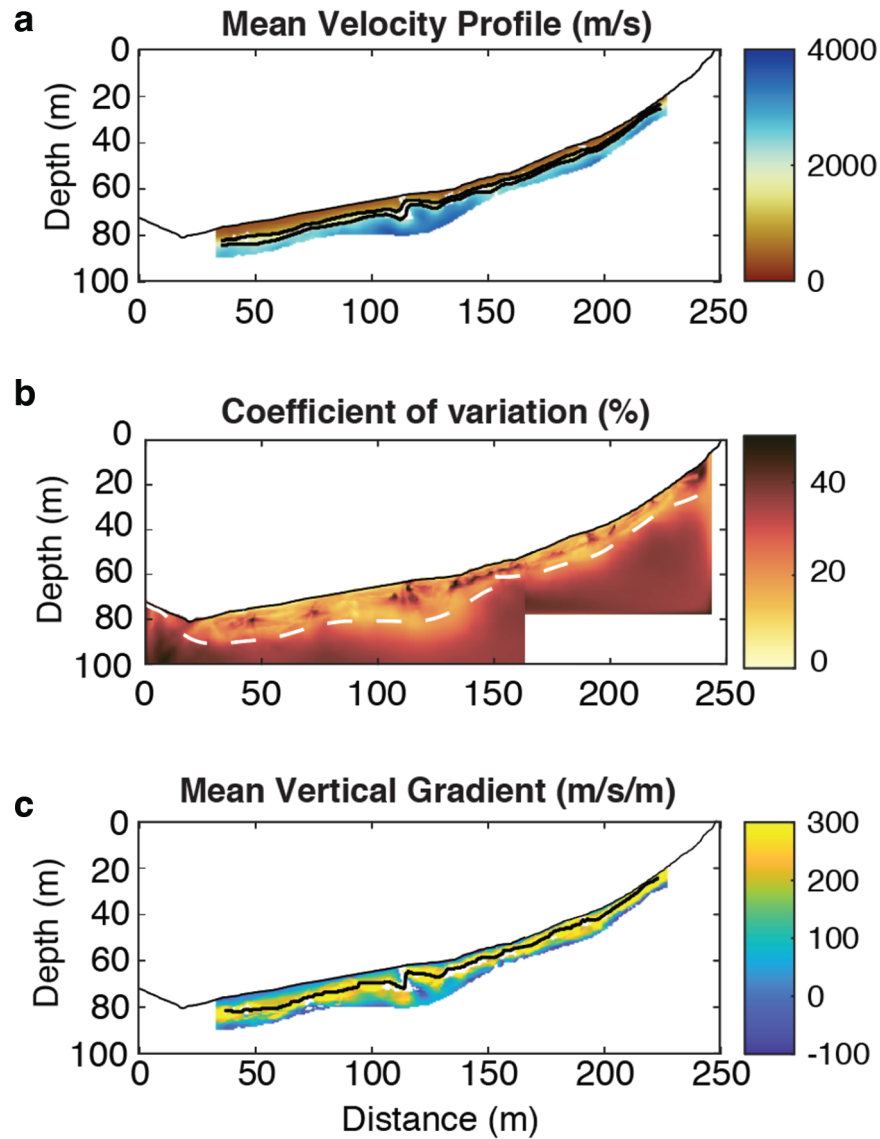


**Figure S6.** Results of Lines 10 and 11 (a-c) inversion using THB rj-MCMC (Huang et al., 2021). (a) Mean velocity model with contour lines at 1000, 2000, 3000, and 4000 m/s. The model is masked out where no geophones are present (edges of survey), below the deepest raypath, and where  $\text{CoV} > 30\%$ . (b) Percent CoV with the deepest raypath as the white dashed line. (c) Mean vertical velocity gradient (m/s/m).

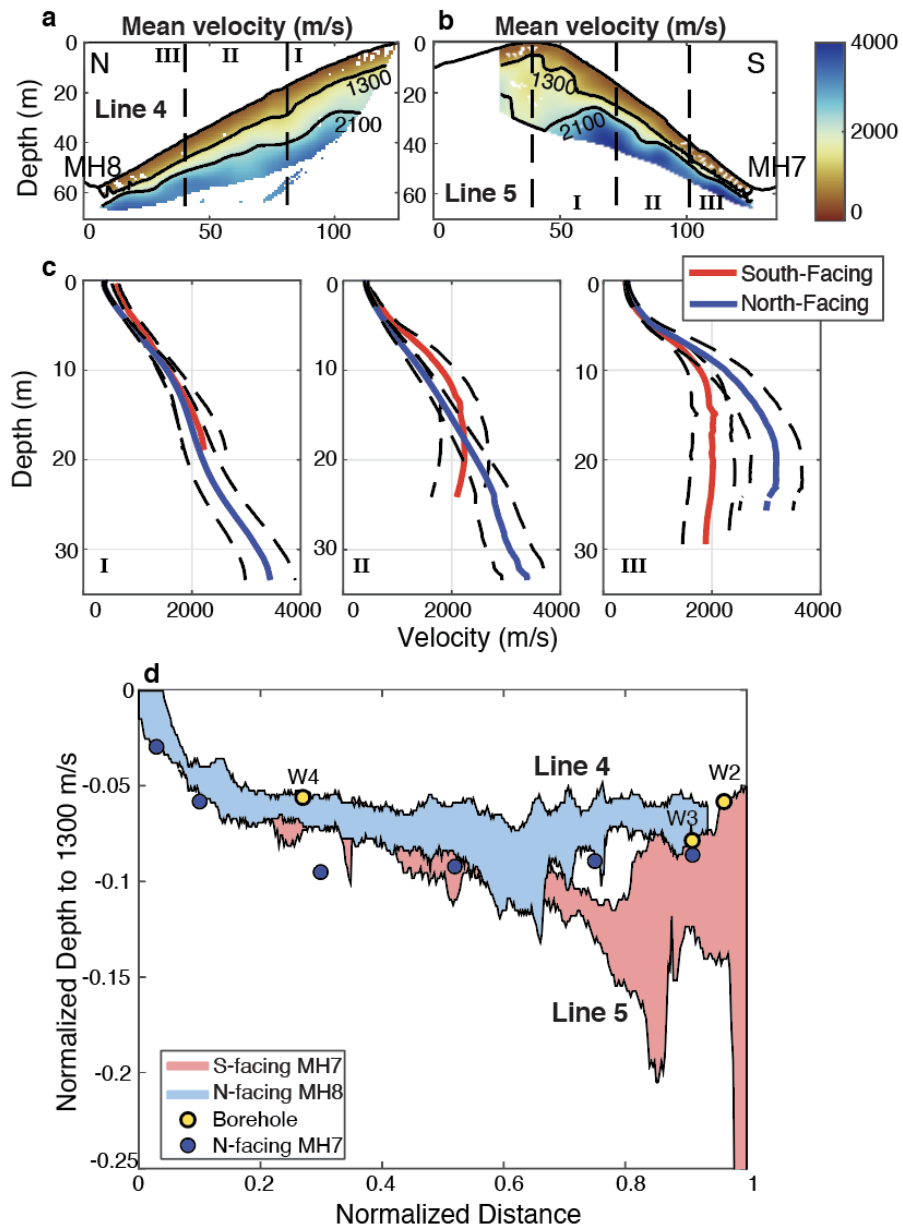


**Figure S7.** Comparison of Interface 2 depth for north- and south-facing hillslopes of Lines 4 and 5 (steepest descent of the slope). Mean velocity profiles for Lines 4 and 5 are shown in (a) and (b), respectively. Contour lines are at the approximate velocities of the Interface 2 (1284 m/s) and Interface 3 (1972 m/s) transitions. Roman numerals indicate three sections of the hillslopes used in (c). (c) shows 1D velocity profiles for three sections of the hillslope for north-facing (blue) and south-facing (red) slopes. Dashed black lines indicate 1 standard deviation. (d) Normalized depth to Interface 2 (1284 m/s contour) with normalized hillslope length. Zero is the channel and one is the ridgetop position. Blue circles represent points where Line 1 intersects a steepest descent transect, since we have no steepest descent survey line for MH7N. Yellow circles represent normalized Interface 2 depth in boreholes MH7-W2, MH7-W3, and MH7-W4.

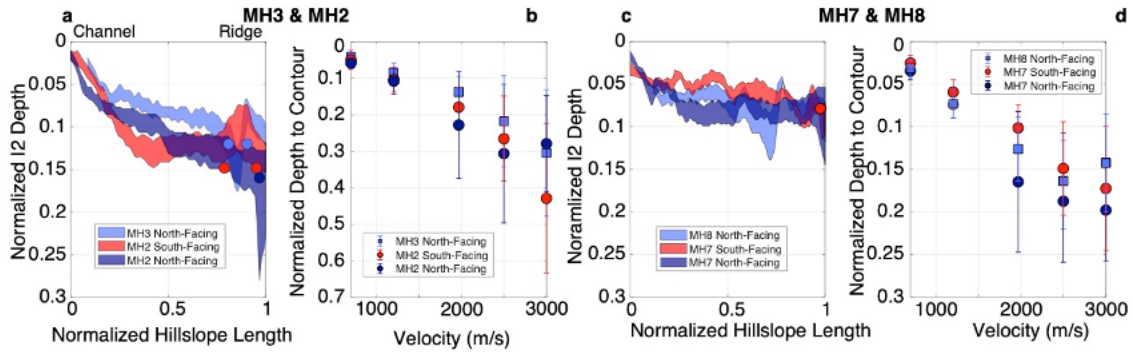


**Figure S8.** Comparison of weathering thickness on north- versus south-facing hillslopes for Line 6 (ab), and Line 1 (cd). Depth to Interface 2 (I2; saprolite-weathered bedrock) with normalized hillslope length (a,c) is shown based on the I2 velocity range ( $1284 \pm 203$  m/s velocity contours). Average depths to various velocity contours are shown normalized to hillslope length in (b, d), including the average Interface 2 velocity contour (1284 m/s) and average Interface 3 velocity contour (1973 m/s).

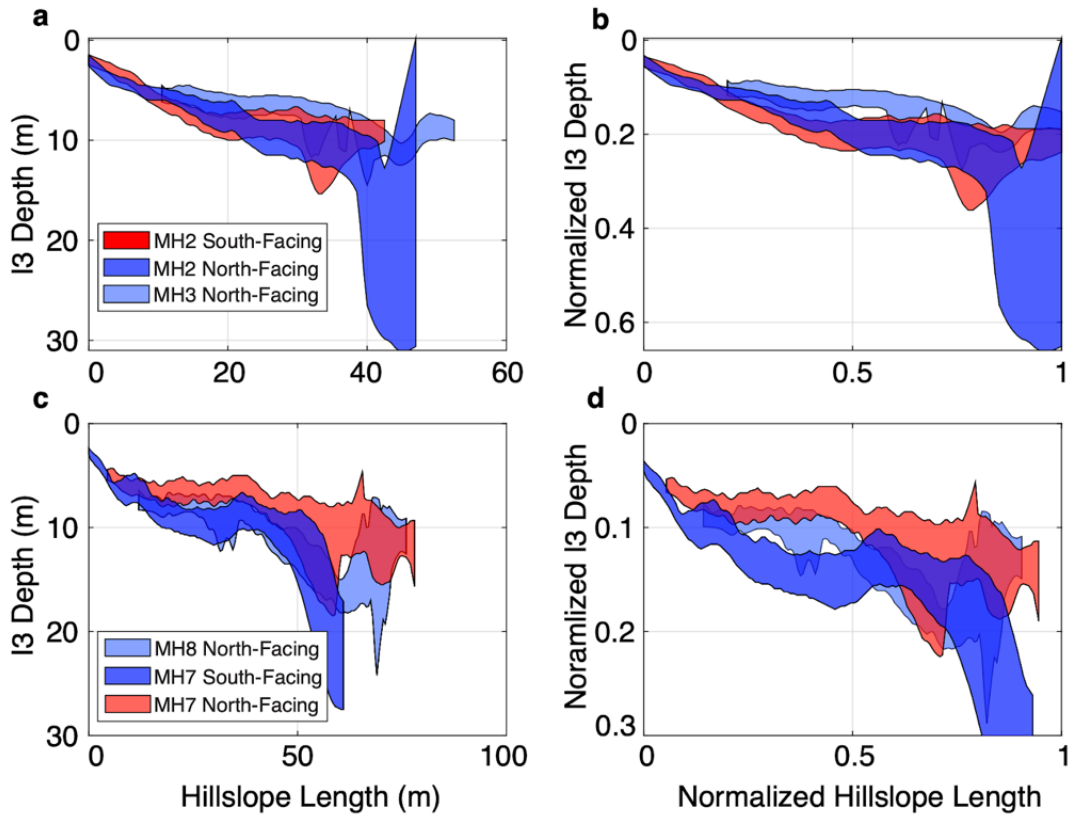


**Figure S9.** Comparison of weathering thickness on north- versus south-facing hillslopes for Line 6 (a-b), and Line 1 (c-d). Depth to Interface 3 (I3; weathered-unweathered bedrock transition) with hillslope length is shown based on the 1972 m/s velocity contour. (b,d) represent the same as (a,c), but hillslope length and depth to I3 are normalized by the hillslope length.

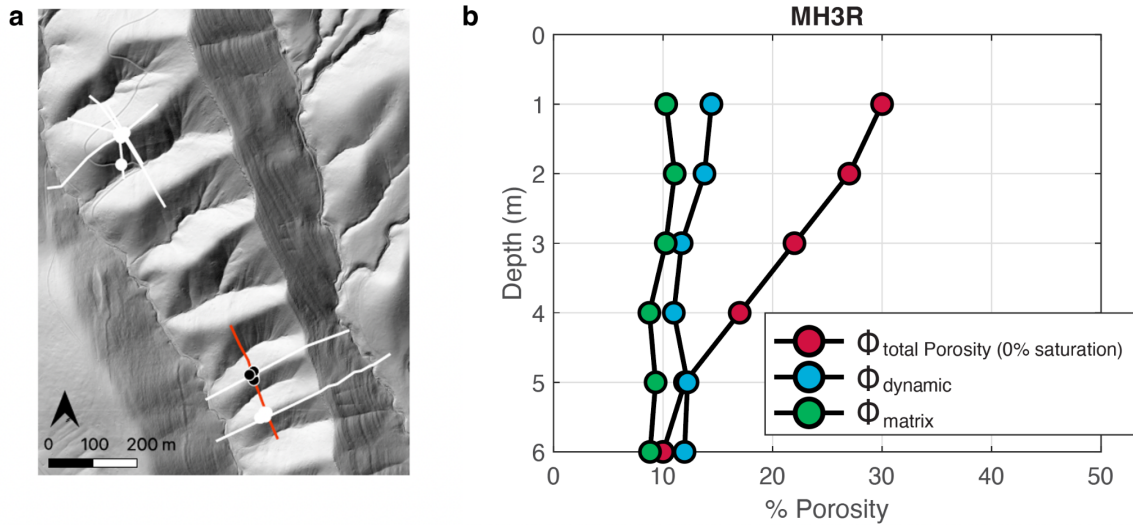


**Figure S10.** 1D rock physics model at MH3R (Line 7). **(a)** Location of Line 7 (red line) and the boreholes used to measure volumetric water content (black circles). **(b)** Porosity with depth from the rock physics model ( $\Phi_{total}$ ) based on the average velocity profile across all wells at MH3R. Measured matrix porosity ( $\Phi_{matrix}$ ) from cores at MH3-W2, MH3-W4, and MH3-W4, interpolated to a 1m depth is shown in green. The dynamic porosity ( $\Phi_{dynamic}$ ) is based on neutron probe measurements at MH7-W2 and MH7-W3, with outliers removed and also interpolated to 1m depth.

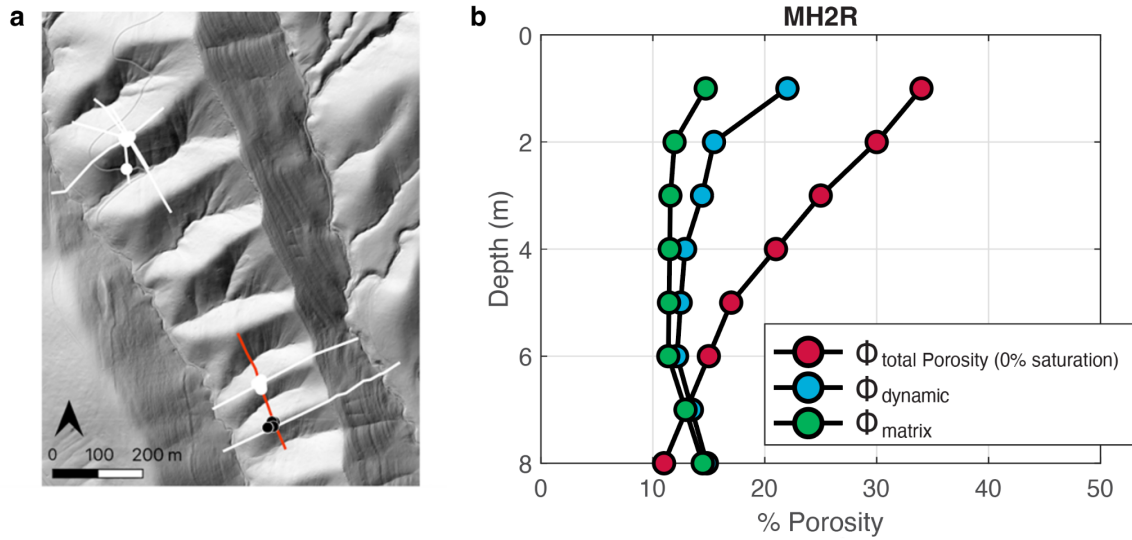


**Figure S11.** 1D rock physics model at MH2R (Line 7). **(a)** Location of Line 7 (red line) and the boreholes used to measure volumetric water content (black circles). **(b)** Porosity with depth from the rock physics model ( $\Phi_{\text{total}}$ ) based on the average velocity profile across all wells at MH2R. Measured matrix porosity ( $\Phi_{\text{matrix}}$ ) from cores at MH7-W1, MH7-W2, and MH7-W3, interpolated to a 1m depth is shown in green. The dynamic porosity ( $\Phi_{\text{dynamic}}$ ) is based on neutron probe measurements at MH3-W6 and MH3-W7, with outliers removed and also interpolated to 1m depth.

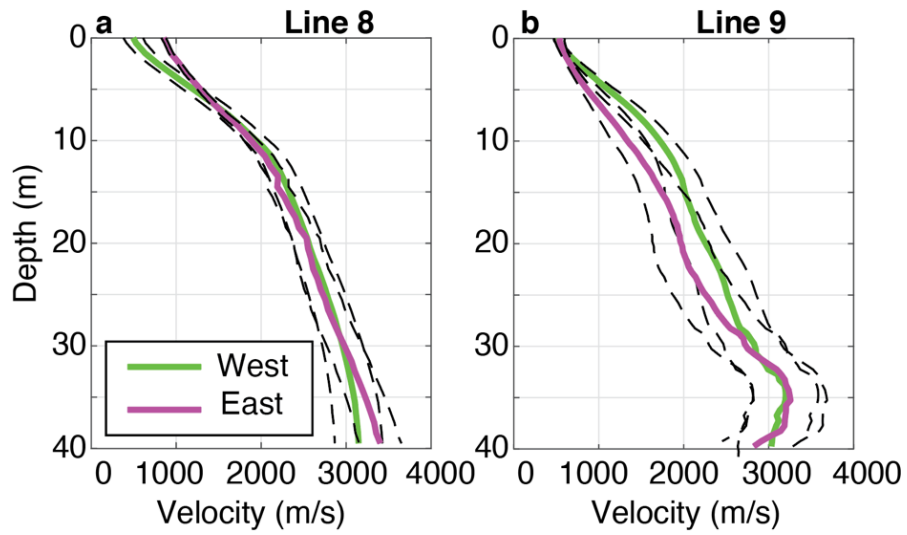


**Figure S12.** Average 1D velocity profile across the entire west-facing (green) and east-facing (pink) slopes for Lines 8 (a) and 9 (b). Dashed black lines represent 1 standard deviation.

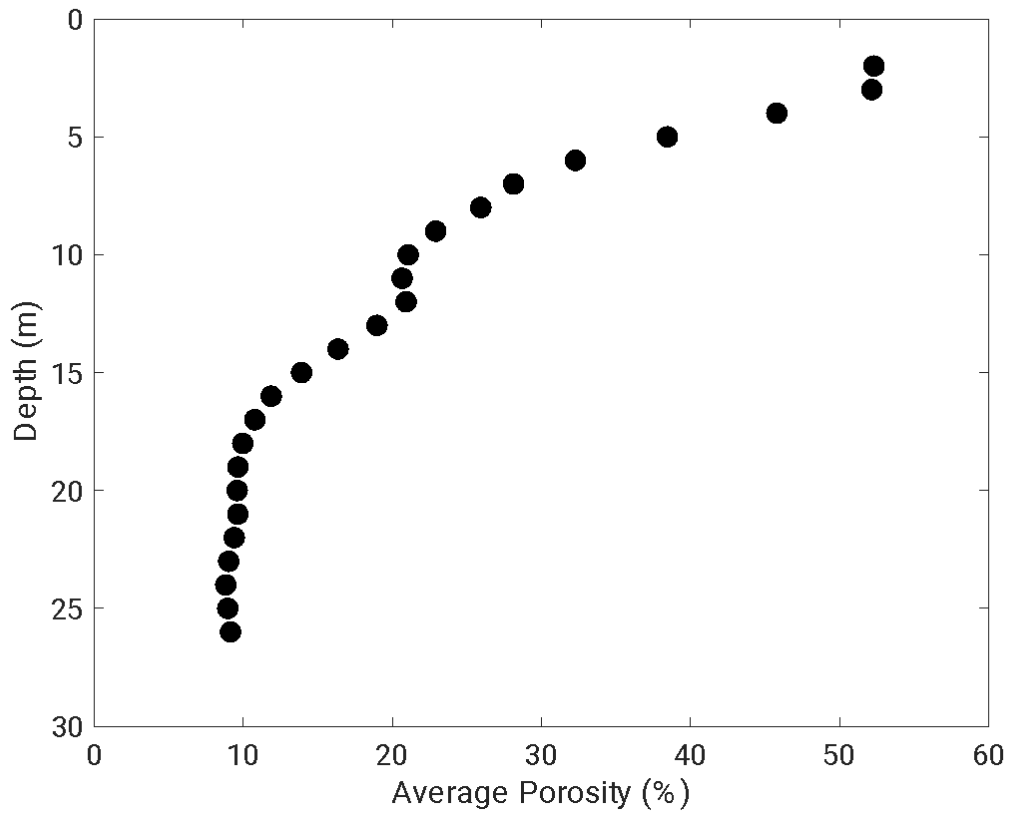


**Figure S13.** Average porosity with depth for the MH7R ridgetop (Line 1). Porosity values were averaged across 180-200 m horizontal distance of the 2D model (**Figure 12**).

**Table S1.** List of model parameters used in different seismic refraction survey lines.

Survey Line	Date	Geophone Number, Spacing (m)	Grid Size (m)	Markov Chains	Iterations	Mean misfit (ms)	Std. Dev. of Misfit (ms)	Noise Hyper-parameter (ms)
Line 1	08/2019	24, 3	0.5	10	$1.5 \times 10^6$	1.23	1.6	1.47
Line 2	08/2021	48, 3	0.25	100	$1.2 \times 10^6$	0.84	1.09	1.09
Line 3	08/2019	24, 3	0.5	15	$1.0 \times 10^6$	1.67	2.13	2.00
Line 4	08/2021	48, 3	0.25	100	$1.5 \times 10^6$	1.30	1.70	1.23
Line 5	08/2021	48, 2.5	0.25	100	$1.5 \times 10^6$	1.16	1.47	1.16
Line 6	08/2021	48, 2	0.25	18	$1.3 \times 10^6$	0.89	1.17	1.05
Line 7	12/2019	24, 3	0.5	15	$1.2 \times 10^6$	1.14	1.64	1.62
Line 8	08/2021	48, 5	1	10	$0.7 \times 10^6$	1.75	2.25	2.23
Line 9	01/2018	72, 2	0.5	15	$2.9 \times 10^6$	1.35	1.85	1.5-1.8
Line 10/11	12/2019	24, 3	0.5	10	$0.8 \times 10^6$ / $1.0 \times 10^6$	1.29/0.96	1.78/1.23	1.70/1.20

**Table S2.** Elastic moduli for minerals used in rock physics models (Mavko et al., 2009; Gu et al., 2020s).

Mineral	Bulk Modulus (Pa)	Shear Modulus (Pa)
Quartz	$37 \times 10^9$	$44 \times 10^9$
Feldspar	$37.5 \times 10^9$	$15 \times 10^9$
Illite	$52.3 \times 10^9$	$31.7 \times 10^9$